energy&fuels

pubs.acs.org/EF

Article

Optimizing Reduced Graphene Oxide Aerogel for a Supercapacitor

Soon Poh Lee, Gomaa A.M. Ali, H.H. Hegazy, Hong Ngee Lim, and Kwok Feng Chong*

Cite This: https://dx.doi.org/10.1021/acs.energyfuels.0c04126

Read Online

ACCESS | Metrics & More | Article Recommendations | Supporting Information

ABSTRACT: Reduce graphene oxide (rGO) aerogels with different precursor graphene oxide sheet sizes are synthesized using L-ascorbic acid reduction followed by an ambient pressure drying method. The sheet sizes determine the oxygen functionality content during aerogel formation, which subsequently affect its structural properties. The optimized sheet size renders strong parallel sheet stacking to provide mechanical strength that withstands capillary action during aerogel formation with a high surface area (190.40 m^2 g^{-1}) and pore volume (0.261 cm^3 g^{-1}). Such surface properties enhance the electrochemical properties of rGO aerogel (182 F g^{-1} at 0.75 A g^{-1}) and render it to be an excellent electrode material for a supercapacitor.

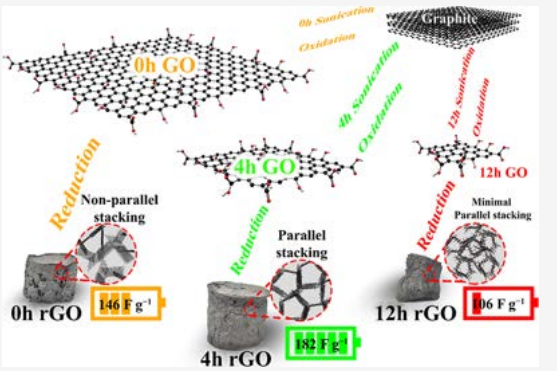

INTRODUCTION

The global revolution in fulfilling human needs requires huge energy consumption. In this context, an energy storage device plays a vital role in ensuring uninterrupted energy supply. Currently, a battery and supercapacitor are the well-known energy storage devices with different energy-storing mechanisms but complement each other in the storage performance.[1] A Li-ion battery (LIB) excels in providing high energy density but suffers from poor long-term stability and power density.[2] In contrast, a supercapacitor can surmount the constraint of an LIB except on the energy density performance where amelioration is still available.[3,4] The literature shows that nanocomposite pseudocapacitors undergo redox reaction, which can increase the energy storage with a minimal stability reduction.[5−8] In addition, electrochemical double-layer capacitors (EDLCs) show exceptionally high cycling stability and fast charging ability among the energy storage devices, and their capacitance performance could be enhanced by tuning the properties of an electrode material.[9−11] The chemically derived graphene, or better known as reduced graphene oxide (rGO), has been widely studied as an energy storage material due to its high conductivity and excellent double-layer capacitance behavior. The production of rGO requires the reduction of graphene oxide (GO), which is conventionally achieved by a strong reducing agent such as hydrazine. The hazardous nature of hydrazine prompts the usage of green chemicals such as L-ascorbic acid, and it is proven that the reduction efficacy of L-ascorbic acid is comparable to hydrazine reduced GO or hydrothermal reduced GO.[12,13] The rGO in an aerogel form has been proposed as the supercapacitor electrode due to its high surface area and porosity that enable the easy access of electrolyte ions.[14,15] Various approaches have been adopted to enhance rGO aerogel as a supercapacitor electrode, such as aerogel composite formation with metal oxides/polymers, functionalization of rGO, and heteroatom doping in rGO aerogel.[16−22] The strategy of doping heteroatoms such as nitrogen, sulfur, or boron in rGO aims to improve the electrical properties as well as contribute to the supercapacitor performance *via* pseudocapacitive heteroatoms.[19−21] The modification of rGO by adding metal oxides such as SnO_2 and $W_{18}O_{49}$, functionalization of rGO with fluorophenylene group or phosphorus, and rGO composite formation with PEDOT:PSS or MnO_2 are proven to improve the supercapacitor performance by enhancing the electrolyte transport and creating additional electrochemical active sites for charge storage.[16−18,22−24] However, these strategies require multiple steps and often demand additional chemicals to be added in the process. Thus, it is important to study the intrinsic properties of rGO in the aerogel formation. The correlation between its intrinsic properties such as sheet size and the aerogel electrochemical properties is vital in the roadmap of developing a high-performance supercapacitor. So far, only the flake size effect on rGO aerogel mechanical strength has been reported elsewhere.[25]

In this study, a low-cost and industrial-scale feasible approach is used to produce rGO aerogel. GO, as the aerogel precursor, was produced at different sheet sizes and subsequently used for the aerogel formation by ambient

Received: December 8, 2020
Revised: February 10, 2021

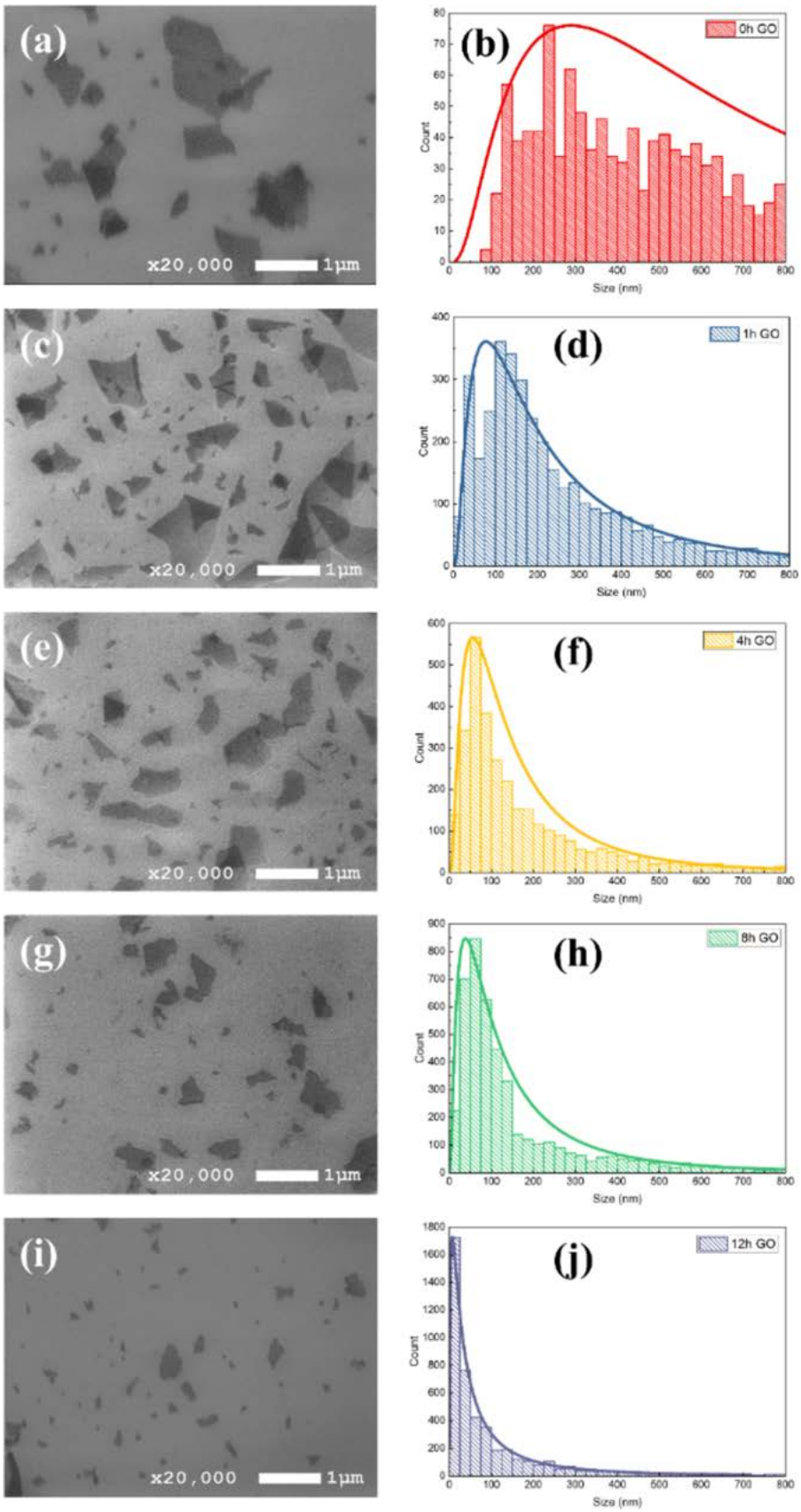

Figure 1. GO sheets under FESEM analysis and size distribution for (a,b) 0, (c,d) 1, (e,f) 4, (g,h) 8, and (i,j) 12 h GO.

pressure drying. We establish the systematic correlation between the GO sheet size and the electrochemical properties of the assembled aerogel. The findings could facilitate the production of graphene aerogel with ameliorated energy

https://dx.doi.org/10.1021/acs.energyfuels.0c04126
Energy Fuels XXXX, XXX, XXX−XXX

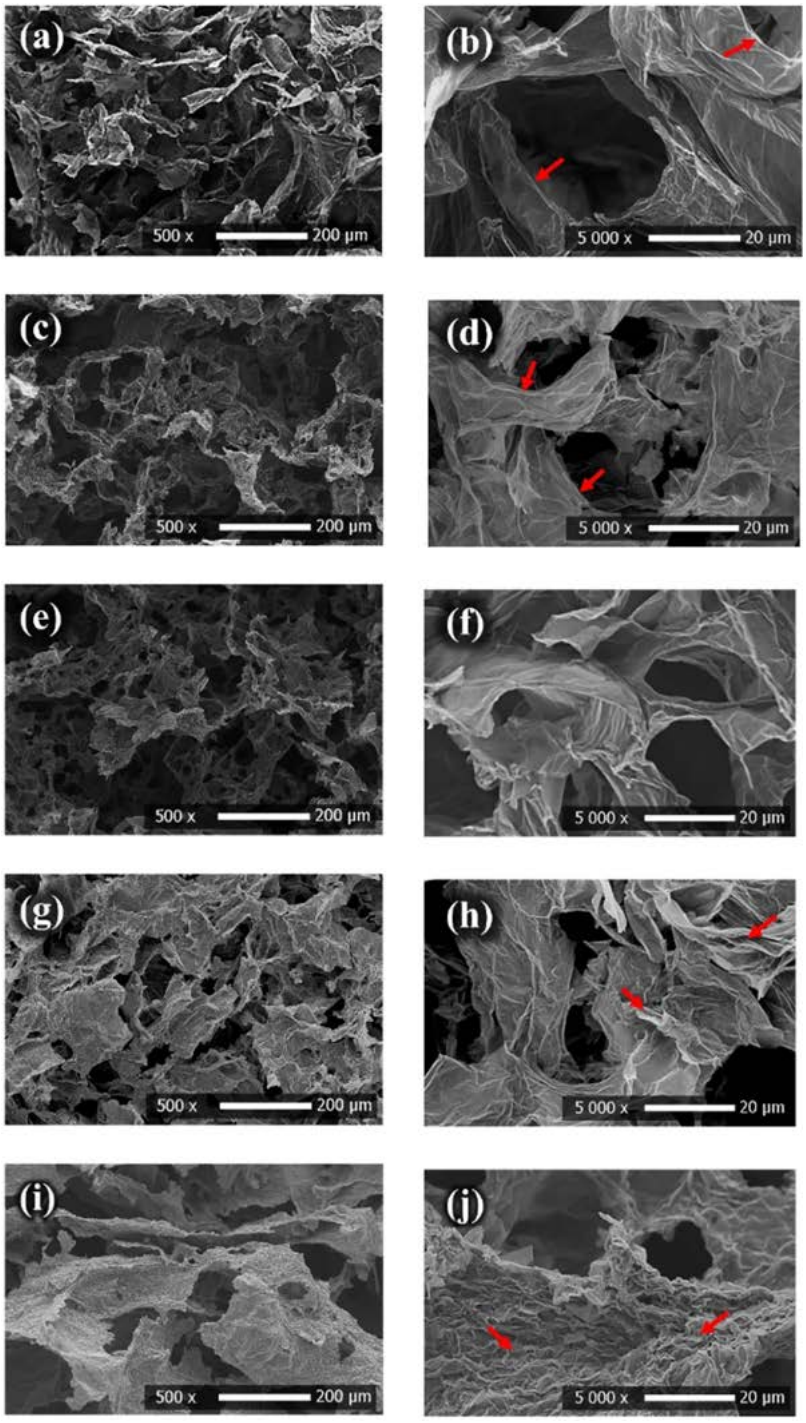

Figure 2. SEM images at 500× and 5000× for (a,b) 0, (c,d) 1, (e,f) 4, (g,h) 8, and (i,j) 12 h rGO. Red arrows are pointing to the bending and crumpled zones of rGO. Additional SEM images are shown in Figure S2.

storage performance by harnessing the intrinsic properties of GO sheets.

EXPERIMENTAL SECTION

Preparation of rGO Aerogel. The synthesis of different sheet sizes of GO as a starting material was shown in our previous study.[26] Typically, 4 g of graphite flake (+100 mesh, Graphene Supermarket) was preoxidized with a mixture of 60 mL of H_2SO_4 (95.0−98.0%, J.T. Baker), 6 g of $K_2S_2O_8$ (Sigma-Aldrich), and 6 g of P_2O_5 (Sigma-Aldrich) at 80 °C for 6 h. The resultant product was then diluted and washed with deionized water until the pH was neutral. Sonication was done for the targeted duration to produce different sheet sizes followed by oxidation using 35 g of $KMnO_4$ (R&M Chemicals) in 300 mL of H_2SO_4 for 4 h at 35 °C under stirring. The mixture was diluted with 700 mL deionized water, and the oxidation was stopped with 100 mL H_2O_2 (30%, HmbG Chemicals). Centrifugation was applied to wash the mixture with 2 L of 1:10 HCl (37%, Merck) followed by excess deionized water until the pH was neutral. Graphite oxide was obtained after freeze-drying and exfoliated through sonication into GO.

rGO aerogel was produced by adopting and modifying the method proposed by Yang et al.[27] First, 80 mg of L-ascorbic acid (L-AA) (HmbG Chemicals) was added into 10 mL of GO dispersion (4 mg

https://dx.doi.org/10.1021/acs.energyfuels.0c04126
Energy Fuels XXXX, XXX, XXX−XXX

mL^{-1}) and heated at 80 °C for 80 min. A mass ratio of 2:1 for L-AA:GO was used as it had been proven to produce rGO aerogel with optimum structural properties.[27,28] The partially reduced graphene hydrogel was frozen at −18 °C followed by heating at 80 °C for 8 h for further reduction. The resultant hydrogel was washed with deionized water to remove excess reactants. rGO aerogel was obtained after oven-drying the hydrogel at 60 °C for 24 h. According to sonication duration, the rGO aerogel samples were termed as 0, 1, 4, 8, and 12 h rGO to indicate the no sonication, 1, 4, 8, and 12 h sonication times, respectively.

Materials Characterization. The sheet sizes of GO were determined using a field emission scanning electron microscope (FESEM, JEOL JSM-7800F), and an average of 2500 sheets was used for each sample for the sheet size determination. The morphology and elemental composition of rGO aerogel were studied by a scanning electron microscope with an energy-dispersive X-ray analysis (SEM−EDX, FEI Quanta 450). The crystal structure of rGO aerogel was obtained by X-ray diffraction (XRD, Rigaku Miniflex II) for 2θ from 3 to 80°. The surface area and porosity of the rGO aerogel were experimented by a N_2 adsorption−desorption isotherm using a Micromeritics ASAP 2020 at 77 K with a degassing temperature at 120 °C.

Electrochemical Measurements. The working electrode was prepared by pressing a thin layer of rGO aerogel sample (0.7−1.3 mg) onto nickel foam. All the current reported in this work was normalized against a sample mass. A three-electrode cell system was set up to assess the electrochemical performance using an Autolab M101 at room temperature, with platinum wire as a counter electrode and Ag/AgCl as a reference electrode. KOH (5 M) was used as an electrolyte throughout cyclic voltammetry (CV), galvanostatic charge−discharge (GCD), and electrochemical impedance spectroscopy (EIS) measurements. Previous reports suggest that the concentration of a KOH electrolyte at 5 M provides the lowest charge transfer resistance and highest specific capacitance.[29] Eq 1 was used to calculate the specific capacitance (C_{sp}) from the GCD curve.

$$C_{sp} = \frac{I \times \Delta t}{m \times \Delta V} \quad (1)$$

where I is the discharge current, Δt is the discharge time, m is the mass of sample, and ΔV is the potential window.

RESULTS AND DISCUSSION

Structural and Morphological Analyses. GO as the precursor for rGO aerogel formation was fragmented into different sheet sizes with ultrasonication. Figure 1 shows the GO sheet distribution on a Si wafer under FESEM observation. The mean sheet size distributions for each GO sample are computed to be 290.29, 80.08, 60.06, 40.04, and 10.01 nm for 0, 1, 4, 8, and 12 h GO, respectively. It shows that the prolonged sonication produces GO sheets with a smaller sheet size, which had been reported in our previous study.[26] Typically, GO sheet fragmentation occurs at the atomic level, and it is accompanied by the rise of localized temperature and pressure during sonication.[30] A smaller sheet size of GO creates a higher active surface area for localized heat oxidation to take place, which subsequently produces higher oxygen functionalities at the GO sheets. These results corroborate well with our previous FTIR analysis, where GO with a smaller sheet size possesses more edge oxygen functionalities.[26]

Table 1. EDX Results for wt % of C and O Contents in rGO Aerogel Samples

sample	C (wt %)	O (wt %)	C/O
0 h rGO	82.82	17.18	4.82
1 h rGO	81.42	18.58	4.38
4 h rGO	81.10	18.90	4.29
8 h rGO	80.47	19.53	4.12
12 h rGO	79.41	20.59	3.86

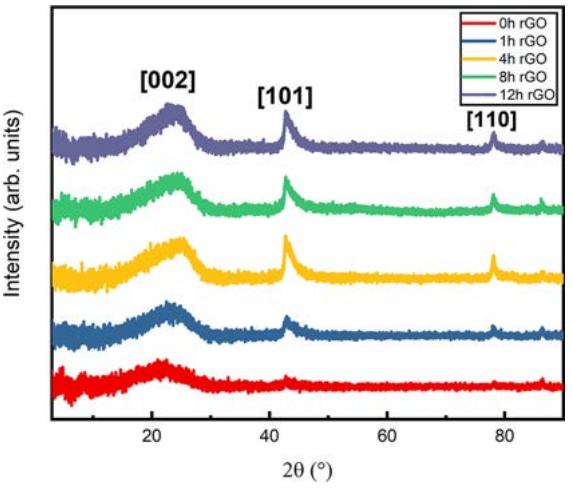

Figure 3. XRD patterns for 0, 1, 4, 8, and 12 h rGO.

Table 2. Peak Ratio for the XRD Pattern for (002) and (101) Peaks for the Different Sheet Sizes of rGO Aerogel Samples

sample	peak (002)	peak (101)	ratio ((002)/(101))
0 h rGO	1343.19	91.28	14.72:1
1 h rGO	1616.91	270.53	5.98:1
4 h rGO	2288.51	618.68	3.70:1
8 h rGO	2012.45	537.82	3.74:1
12 h rGO	2279.11	527.07	4.32:1

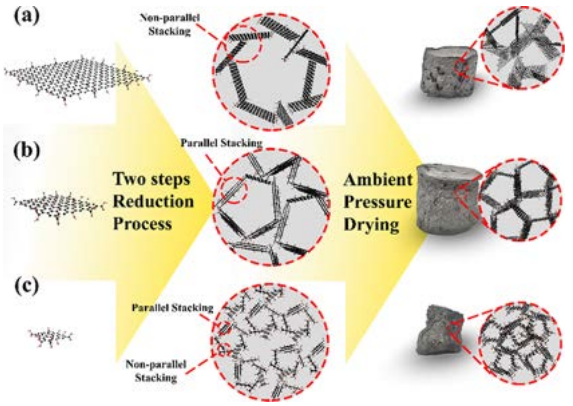

Figure 4. Schematic diagram of the rGO aerogel formation for (a) 0 and 1; (b) 4; and (c) 8 and 12 h rGO.

The fragmented GO sheets were subjected to L-AA reduction and ambient pressure drying to produce rGO aerogel. The process of aerogel formation started with GO sheet stacking to form a strong structure, followed by oxygen functionality removal to form rGO, and ended with water removal. The FTIR analysis (Figure S1) confirms that the as-prepared rGO aerogel is free from L-AA residue, which is consistent to the previous report on rGO reduced by L-AA.[12,31] The as-prepared rGO aerogel samples were investigated by a scanning electron microscope to study their morphological properties (Figure 2). The strong capillary action of water removal during the drying process causes the final pore formation in rGO aerogel, as seen in 4 h rGO aerogel, where

https://dx.doi.org/10.1021/acs.energyfuels.0c04126
Energy Fuels XXXX, XXX, XXX−XXX

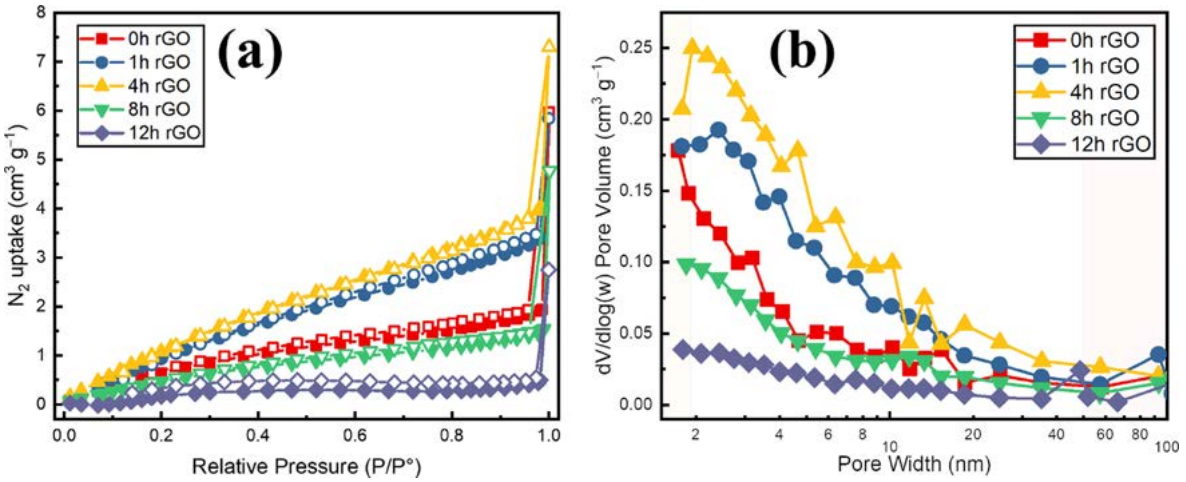

Figure 5. (a) N_2 adsorption−desorption isotherm (a closed symbol represents the adsorption curve, while an open symbol represents the desorption curve) and (b) pore size distribution. The light yellow region indicated the microporous region and white space for mesoporous while light pink refers to a macroporous region.

Table 3. Surface Area and Pore Volume for rGO Samples

sample	BET surface area (m^2 g^{-1})	pore volume (cm^3 g^{-1})
0 h rGO aerogel	107.20	0.087
1 h rGO aerogel	171.60	0.179
4 h rGO aerogel	190.40	0.261
8 h rGO aerogel	79.05	0.069
12 h rGO aerogel	30.81	0.026

interconnected pores can be observed. For larger sheets (0 and 1 h rGO), the rGO sheets exhibit bending and twisting at the edge with pore deformation. On the other hand, at the smaller sheets (8 and 12 h rGO), a compact and crumpled morphology can be observed, possibly due to the higher oxygen functionalities in smaller sheets. Furthermore, the freezing of hydrogel with a smaller sheet size at a partially reduced state also causes the pore cracking and deformation, instead of strengthening the wall of pores.[25,27] The porous wall of aerogel for 4 h rGO shows relatively less crumple and reflects the several stacking layers of the rGO sheet that increases the mechanical strength of the aerogel structure for interconnected pore formation. Table 1 shows the C/O wt % of each rGO aerogel sample and indicates that oxygen remains after reduction, which supports the proposed gelation by oxygen functionalities, as suggested in other works.[32−34] As the sheet size decreases, the oxygen functionalities increase and therefore leads to a stronger sheet interaction *via* hydrogen bonding that produces the higher mechanical strength of the aerogel. However, the morphological observation only supports this statement up to 4 h rGO where smaller rGO sheet samples (8 and 12 h rGO) exhibit pore cracking and deformation. For this, XRD analyses were later employed to investigate the rGO sheet stacking behavior.

XRD analyses (Figure 3) show that all rGO aerogel samples exhibit major peaks at ca. 2θ = 25.4, 42.68, and 78.13°, which are attributable to the diffraction planes of the graphitic carbon of (002), (101), and (110), respectively. Accounting on the (002) peak, all rGO aerogel samples show the interlayer spacing (d) of ca. 3.50 Å, which indicates the oxygen functionality removal from GO (2θ = 10.27°, d = 9.05 Å).[26] The peak broadening could be due to the multimode feature of the interlayer spacing of rGO aerogel[35] and disordered rGO sheets in the aerogel.[36] The interaction between rGO sheets can be divided into parallel and nonparallel stacking, where the former is the adjacent sheet stacking, and the latter is caused by the edge to basal sheet stacking. The parallel and nonparallel stacking can be indicated by the peaks (101) and (002), respectively.[32] Table 2 shows the peak area ratios between (002) and (101), where a higher ratio signifies more nonparallel sheet stacking. The larger sheet samples (0 and 1 h rGO) show more nonparallel sheet stacking, possibly due to lower oxygen functionalities, which limits the intersheet hydrogen bonding and causes random sheet stacking. The 4 h rGO sample shows the highest parallel stacking (lowest peak area ratio (002)/(101)). The high reactivity of oxygen functionalities at the edges of the sheets on 4 h rGO causes strong hydrogen bonding that forms parallel sheet stacking. Further reducing the sheet size for 8 and 12 h rGO, the sheets are so small that they tend to orient randomly, causing the edge plane oxygen groups to interact with basal plane oxygen groups. The XPS analysis reported elsewhere suggests that the smaller sheet size of GO possesses higher edge plane oxygen functionalities (C═O and O−C═O peaks) as compared to the larger sheet size of GO.[37] In addition, the nonparallel stacking in 8 and 12 h rGO is corroborated by SEM observation where crumpled sheets are formed. The different sheet sizes in aerogel formation are best illustrated in Figure 4. The strong sheet stacking caused by the parallel stacking provides mechanical strength to withstand the capillary action of water removal during aerogel formation and exhibits an interconnected pore structure as seen in 4 h rGO.

The N_2 adsorption−desorption isotherm as shown in Figure 5a reflects that all samples behave as a type II isotherm model with the unrestricted monolayer−multilayer adsorption of N_2 on the rGO sheet surface in the aerogel.[38] The N_2 adsorption volume without an observable steep increase (gradual curvature) at the low $P/P°$ region indicates the significant overlapping of a monolayer and initiation of multilayer adsorption.[39] The sudden increase of adsorption volume at the $P/P°$ ca. 1 shows that a macroporous structure and adsorbed multilayer N_2 exists to increase without limit.[39] A minor H4 hysteresis that is observed at $P/P°$ > 0.2 shows the presence of a micromesoporous structure. The 4 h rGO shows the highest surface area (190.40 m^2 g^{-1}) and pore volume

https://dx.doi.org/10.1021/acs.energyfuels.0c04126
Energy Fuels XXXX, XXX, XXX−XXX

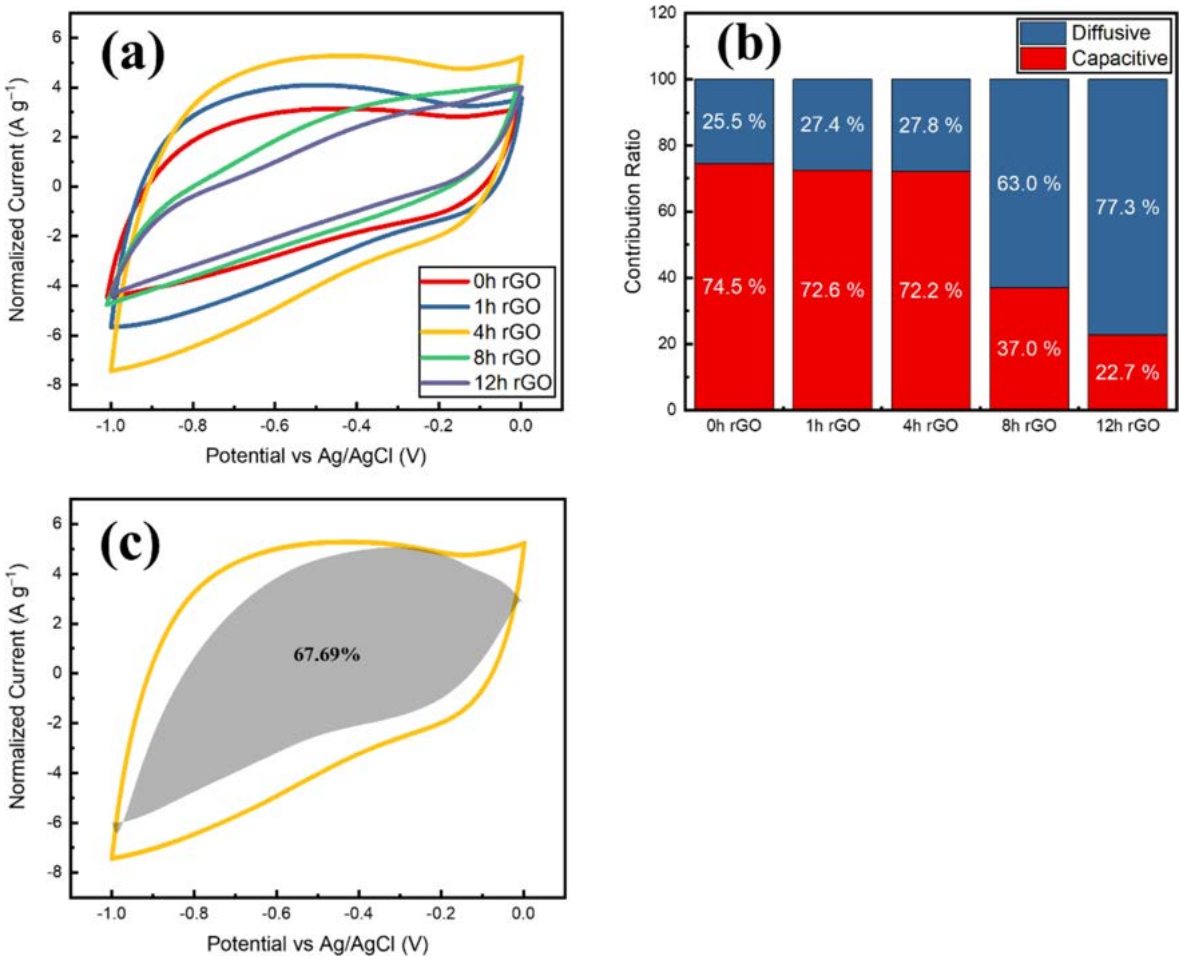

Figure 6. (a) CV curve at 25 mV s^{-1}; (b) Trasatti's analysis to show diffusive and capacitive contribution; and (c) Dunn's analysis for 4 h rGO representing the area for EDLC behavior in the CV.

(0.261 cm^3 g^{-1}) as compared to other rGO aerogel samples in the micromesoporous region as shown in the pore size distribution (Figure 5b). The detailed surface area and pore volume of rGO aerogel samples are tabulated in Table 3. The surface area findings corroborate the morphological findings where 4 h rGO with interconnected pores possesses a higher surface area and pore volume, while the pore deformation in other samples causes the lower surface area as well as pore volume.

Electrochemical Performance. The electrochemical properties of different rGO aerogel samples were investigated using CV. The nickel foam was used as a current collector due to its high conductivity and microporous structure that provides the excellent mass transport of an electrolyte.[40] The usage of nickel foam does not give a significant response in CV as compared that for the rGO aerogel samples (Figure S3). Figure 6a shows the CV curves where all samples exhibit an EDLC behavior by showing a rectangular CV shape with a large area under the curve. The area under the curve acts as an indicator for an EDLC effect, where it increases from 0 to 4 h rGO as the sheet size decreases. However, the EDLC effect drops for 8 and 12 h rGO. These findings correlate to the surface area analysis that shows the increasing surface area and pore volume from 0 to 4 h rGO and decreasing from 8 and 12 h rGO. Furthermore, the CV curves of 8 and 12 h rGO slightly deviate from the rectangular shape. This shows the weak charge propagation in 8 and 12 h rGO, possibly due to the higher oxygen functionalities that may alter the charge storage mechanism. For this, further investigation with Trasatti's analysis was conducted[41,42] (detailed calculation is presented in the Supporting Information; and the CV curves of all the samples in different scan rates are shown in Figure S4). Figure 6b shows that the predominant charge storage in 0, 1, and 4 h rGO can be attributed to a capacitive storage. On the other hand, 8 and 12 h rGO show the reversal effect where diffusive storage contributes predominantly to the charge storage mechanism. At a large sheet size, the rGO aerogel samples (0 and 1 h rGO) show a pore deformation that limits the ion diffusion, and the ion adsorption plays a major role in charge storage. As the sheet size decreases (4 h rGO), the aerogel shows the increased surface area and pore volume that enhances the EDLC effect. When the sheet size further decreases (8 and 12 h rGO), the reversal effect occurs where the oxygen functionalities promote the ion diffusions, rather than ion adsorption, and thus making the diffusive storage to be dominant. The Dunn's analysis[43,44] (detailed calculation is presented in the Supporting Information) provides more insight on the contribution of EDLCs. Figure 6c shows the contribution of EDLCs in 4 h rGO. It clearly shows that the EDLC contributes significantly across different potentials. A similar observation is obtained for 0 and 1 h rGO (Figure S7a,b). The EDLC contribution drops significantly for 8 and 12 h rGO (Figure S7c,d), mainly due to the low surface area

https://dx.doi.org/10.1021/acs.energyfuels.0c04126
Energy Fuels XXXX, XXX, XXX−XXX

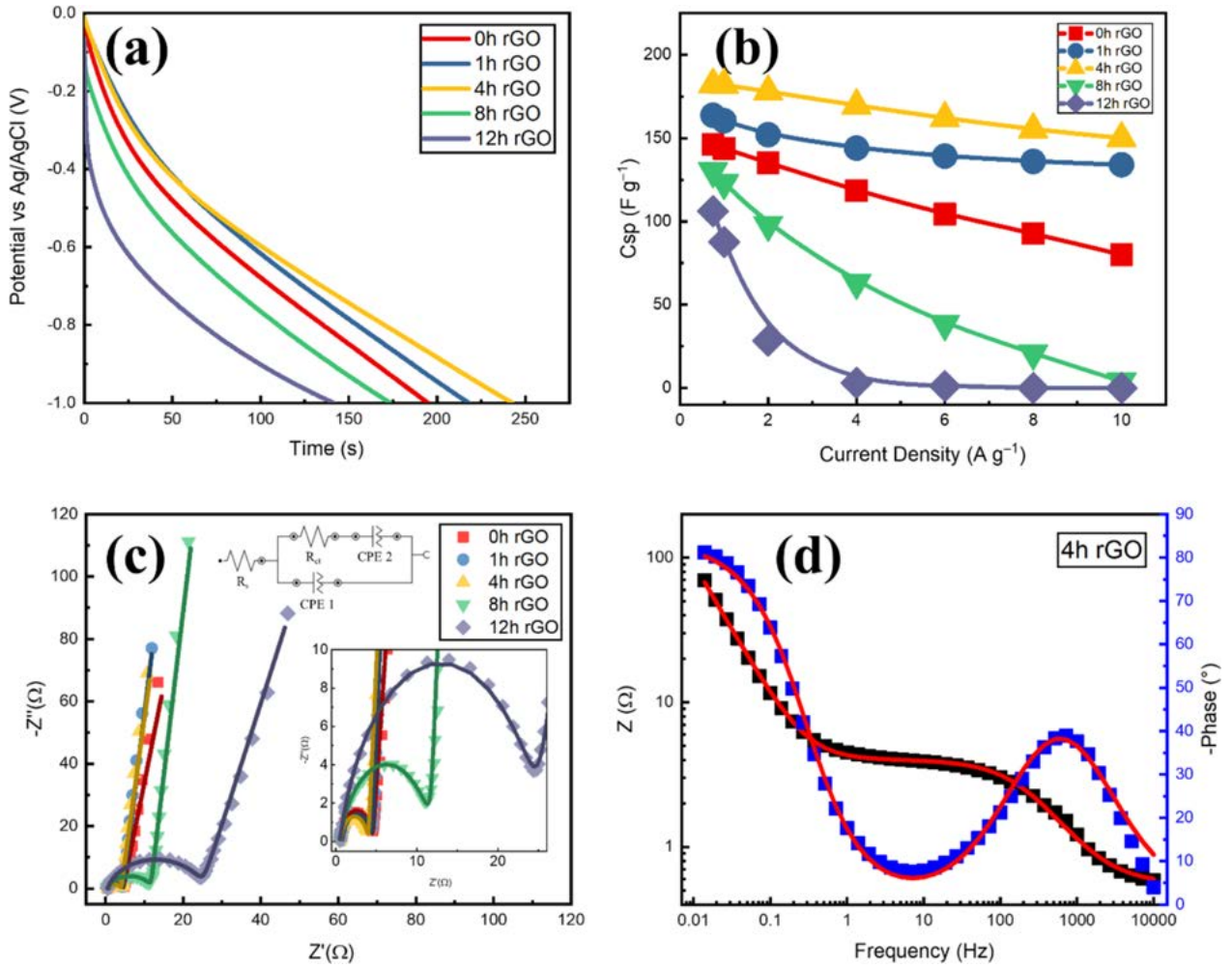

Figure 7. (a) Discharge curves at 0.75 A g^{-1}; (b) variation of specific capacitance with respect to current density; (c) Nyquist plots with the fitted equivalent circuit and high frequency region magnification as insets; and (d) Bode plot for 4 h rGO.

Table 4. Comparison of the Electrochemical Performance for Different rGO Samples

sample	specific capacitance (F g^{-1})	references
exfoliated graphene/MnO_2 composites	106.2 at 0.5 A g^{-1}	45
nanoflake MnO_2/rGO	140.3 at 0.125 A g^{-1}	46
3D cross-linked porous carbon with graphene	141.0 at 0.5 A g^{-1}	47
polyphenylenediamine/rGO composite	158.5 at 1 A g^{-1}	48
$SmCoO_3$/rGO	166.0 at 1 A g^{-1}	49
rGO-S/150 mg MnO_2	169.5 at 1 A g^{-1}	50
rGO-Au@PANI nanocomposite	212.8 at 1 A g^{-1}	51
SnO_2@nitrogen doped graphene	289.4 at 0.5 A g^{-1}	52
4 h rGO aerogel	182.0 at 0.75 A g^{-1}	this work

Table 5. Summary of the Data Fitted with the Equivalent Circuit

sample	R_s (Ω)	R_{ct} (Ω)	CPE1 (F g^{-1})	CPE2 (F g^{-1})	S_E (m^2 g^{-1})
0 h rGO	0.42	4.08	81.95	0.43	412.61
1 h rGO	0.48	3.76	108.50	0.71	572.13
4 h rGO	0.49	2.52	116.87	0.90	593.08
8 h rGO	0.52	11.55	75.23	0.93	375.25
12 h rGO	0.75	24.72	57.18	2.08	295.22

and contribution from ion diffusion, which does not favor ion adsorption in ELDCs.

GCD tests were performed to evaluate the performance of rGO aerogel under the operational condition as a supercapacitor. Figure 7a shows the discharge curves for different aerogel samples. The discharge curve linearity decreases from 0 to 12 h rGO, with significant curve bending from 4 to 12 h rGO. This could be associated to the presence of oxygen functionalities. The specific capacitance (C_{sp}) was computed from the discharge curve slope and summarized in Figure 7b (discharge curves at different current densities for all the samples are shown in Figure S8). The highest capacitance is attained on 4 h rGO with 182 F g^{-1} at 0.75 A g^{-1}, followed by 1 h rGO (164 F g^{-1}), 0 h rGO (146 F g^{-1}), 8 h rGO (130 F g^{-1}), and 12 h rGO (106 F g^{-1}) at the same current density. It is interesting to note that the C_{sp} values drop insignificantly for 0, 1, and 4 h rGO as the current density increases, a clear indication of a strong EDLC effect. For 8 and 12 h rGO, the C_{sp} values increase significantly as the current density decreases. This shows that the diffusive capacitance where ions diffuse extensively at low current density aligns to the findings from Trasatti's analysis. The comparison with other rGO samples is tabulated in Table 4.

The charge kinetics of the rGO aerogel was tested by electrochemical impedance spectroscopy (EIS). Figure 7c

https://dx.doi.org/10.1021/acs.energyfuels.0c04126
Energy Fuels XXXX, XXX, XXX−XXX

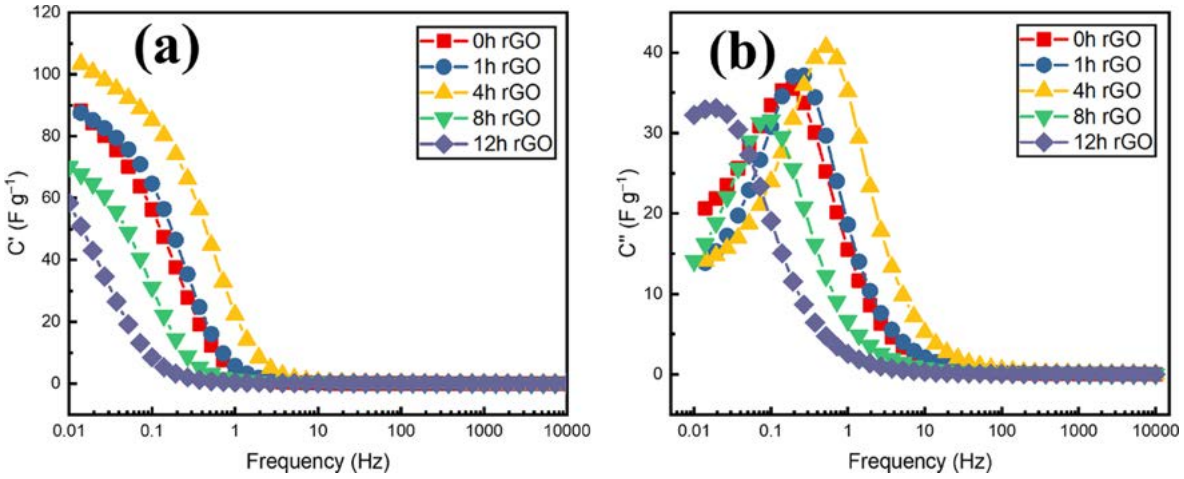

Figure 8. (a) Real and (b) imaginary capacitance plots vs frequency.

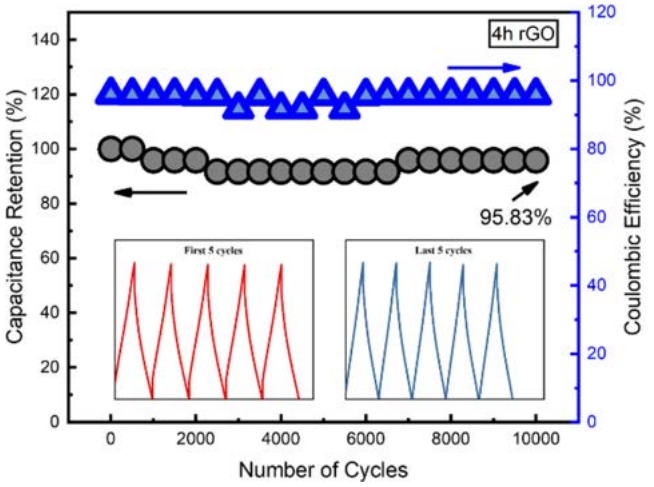

Figure 9. Stability assessment for 4 h rGO with the first and last five cycles of GCD curves as insets.

shows the Nyquist plots for all the rGO aerogel samples with the fitted equivalent circuit as the inset and fitted data as shown in Table 5. As shown in the equivalent circuit, R_s (electrolyte resistance, internal electrode resistance, and contact resistance) is connected in series with both constant phase elements (CPEs), where CPE1 indicates the double-layer capacitance, and CPE2 indicates the diffusive capacitance.[53] The CPE becomes a suitable element in circuit fitting than the capacitor element due to the nonideal capacitive storage mechanism as shown in the CV results.[54] The findings on CPE1 and CPE2 values correlate to Trasatti's analysis, which supports the high double-layer capacitance for 0, 1, and 4 h rGO and high diffusive capacitance for 8 and 12 h rGO. The high R_s and R_{ct} for 8 and 12 h rGO samples suggest that the higher content of oxygen functionalities reduces the electrode conductivity as well as impeding charge transfer, due to the disruption of an sp^2 network in graphene.[55] The electrochemical active surface area (S_E) was further calculated (Table 5) by referring to the imaginary impedance at 10 mHz from the Nyquist plot using eq 2:[41,56]

$$S_E = \frac{C_{dm}}{C_d} \tag{2}$$

where $C_{dm} = (2\pi mfZ'')^{-1}$ and $C_d = 20\ \mu F\ cm^{-2}$ for the carbon material.[57] The findings correlate to the BET analysis where 4 h rGO exhibits the highest S_E of 593.08 $m^2\ g^{-1}$. The high S_E also justifies the high C_{sp} for 4 h rGO. The pore deformation in large sheet aerogels (0 and 1 h rGO) causes the S_E to reduce; meanwhile, pore deformation and the oxygen functionalities cause the further reduction in S_E for smaller sheet-sized aerogels (8 and 12 h rGO). The S_E could explain the charge storage performance where 4 h rGO with the highest S_E exhibits the highest C_{sp}.

The bode plots in Figure 7d describe the relationship between phase angle and frequency, which shows the capacitance effect at a lower frequency. The 4 h rGO shows a good capacitive performance (81.16°), very close to the ideal capacitor phase angle of 90°. The real and imaginary parts of capacitance are calculated and plotted in Figure 8a,b using eqs 3 and 4.

$$C'(\omega) = \frac{-Z''(\omega)}{\omega |Z(\omega)|^2 m} \tag{3}$$

$$C''(\omega) = \frac{Z'(\omega)}{\omega |Z(\omega)|^2 m} \tag{4}$$

where $C'$and C'' are the real and imaginary parts of capacitance, respectively, and $\omega = 2\pi f$. The total capacitance of the sample is the sum of its C' and C'', with the highest capacitance that can be seen on 4 h rGO at all frequency ranges. The relaxation time (τ) is the minimum duration needed to fully discharge with at least 50% efficiency, and it was calculated using eq 5:

$$\tau = 2\pi f^{*-1} \tag{5}$$

where f^* is the frequency at the maximum imaginary capacitance in Figure 8b.[7,41] The result shows that 4 h rGO possesses the shortest time (0.31 s) to have 50% efficiency discharge, as compared to 0 h rGO (0.82 s), 1 h rGO (0.59 s), 8 h rGO (1.59 s), and 12 h rGO (8.24 s). The best performing sample, 4 h rGO, was subjected to continuous GCD for stability assessment. Figure 9 shows that 4 h rGO exhibits as a stable and reliable supercapacitor electrode material, which retains up to 95.83% capacitance after 10,000 cycles at 10 A g^{-1}. Along with the GCD cycles, 4 h rGO is able to maintain the Coulombic efficiency at 95%. The inset of Figure 9 shows the GCD curves for the first and last five cycles of the GCD

https://dx.doi.org/10.1021/acs.energyfuels.0c04126
Energy Fuels XXXX, XXX, XXX−XXX

stability test. It can be deduced that there is no significant difference in the GCD curve shape, further solidifying the claim for its application as a long-term supercapacitor electrode.

CONCLUSIONS

The intrinsic properties of GO as the precursor for rGO aerogel are studied from the perspective of the sheet size. It is discovered that GO sheets tend to form nonparallel stacking during rGO aerogel formation, which leads to a low structural strength and poor surface area. The optimization of GO sheets is proven to effectively tune the GO sheets into parallel stacking during aerogel formation, producing rGO aerogel with a high surface area (190.40 $m^2 g^{-1}$) and pore volume (0.26 $cm^3 g^{-1}$). These structural properties contribute to the electrochemical properties of the optimized rGO aerogel (182 F g^{-1} at 0.75 A g^{-1}) with high stability (95.83% capacitance retention for 10,000 GCD cycles). This study highlights the importance of optimizing GO sheets in the preparation of aerogel for supercapacitor applications.

ASSOCIATED CONTENT

Supporting Information

The Supporting Information is available free of charge at https://pubs.acs.org/doi/10.1021/acs.energyfuels.0c04126.

FTIR spectra for L-AA, hydrazine reduced GO and 4 h rGO, SEM images at 500×, CV curves of bare nickel foam and 4 h rGO, CV curves for rGO aerogel with different scan rates, plots of Trasatti's analysis calculations with detailed capacitive and diffusive contributions, plots of the Dunn's analysis calculations, Dunn's analysis plots for rGO aerogel, and galvanostatic discharge curves with different current densities (PDF)

AUTHOR INFORMATION

Corresponding Author

Kwok Feng Chong − *Faculty of Industrial Sciences & Technology, Universiti Malaysia Pahang, Kuantan 26300, Malaysia;* orcid.org/0000-0003-0786-842X; Email: ckfeng@ump.edu.my; Fax: +609 5492766

Authors

Soon Poh Lee − *Faculty of Industrial Sciences & Technology, Universiti Malaysia Pahang, Kuantan 26300, Malaysia*

Gomaa A.M. Ali − *Chemistry Department, Faculty of Science, Al–Azhar University, Assiut 71524, Egypt*

H.H. Hegazy − *Department of Physics, Faculty of Sciences, King Khalid University, Abha 61413, Saudi Arabia*

Hong Ngee Lim − *Department of Chemistry, Faculty of Science, Universiti Putra Malaysia, UPM Serdang, Selangor 43400, Malaysia;* orcid.org/0000-0003-2436-8953

Complete contact information is available at: https://pubs.acs.org/10.1021/acs.energyfuels.0c04126

Author Contributions

The manuscript was written through contributions of all authors. All authors have given approval to the final version of the manuscript.

Notes

The authors declare no competing financial interest.

ACKNOWLEDGMENTS

The authors would like to acknowledge the funding from the Ministry of Education Malaysia in the form of [RDU1901186: FRGS/1/2019/STG07/UMP/02/6] and the Malaysia Toray Science Foundation grant RDU201502. Moreover, the authors extend their appreciation to the Deanship of Scientific Research at King Khalid University for funding this work through the research group project under grant no. (R.G.P. 2/115/41).

REFERENCES

(1) Lin, Z.; Goikolea, E.; Balducci, A.; Naoi, K.; Taberna, P. L.; Salanne, M.; Yushin, G.; Simon, P. Materials for supercapacitors: When Li-ion battery power is not enough. *Mater. Today* **2018**, *21*, 419−436.

(2) Chiochan, P.; Kosasang, S.; Ma, N.; Duangdangchote, S.; Suktha, P.; Sawangphruk, M. Confining Li_2S_6 catholyte in 3D graphene sponge with ultrahigh total pore volume and oxygen-containing groups for lithium-sulfur batteries. *Carbon* **2020**, *158*, 244−255.

(3) Chen, L.; Wen, Z.; Chen, L.; Wang, W.; Ai, Q.; Hou, G.; Li, Y.; Lou, J.; Ci, L. Nitrogen and sulfur co-doped porous carbon fibers film for flexible symmetric all-solid-state supercapacitors. *Carbon* **2020**, *158*, 456−464.

(4) Kiran, S. K.; Shukla, S.; Struck, A.; Saxena, S. Surface enhanced 3D rGO hybrids and porous rGO nano-networks as high performance supercapacitor electrodes for integrated energy storage devices. *Carbon* **2020**, *158*, 527−535.

(5) Sun, J.; Wang, R.; Yuan, C. MoS3 nanoparticles on reduced graphene oxide. *Mater. Today* **2018**, *21*, 193−194.

(6) Raju, K.; Han, H.; Velusamy, D. B.; Jiang, Q.; Yang, H.; Nkosi, F. P.; Palaniyandy, N.; Makgopa, K.; Bo, Z.; Ozoemena, K. I. Rational design of 2D manganese phosphate hydrate nanosheets as pseudocapacitive electrodes. *ACS Energy Lett.* **2019**, *5*, 23−30.

(7) Sarkar, D.; Das, D.; Das, S.; Kumar, A.; Patil, S.; Nanda, K. K.; Sarma, D. D.; Shukla, A. Expanding interlayer spacing in MoS_2 for realizing an advanced supercapacitor. *ACS Energy Lett.* **2019**, *4*, 1602−1609.

(8) Liu, X.; Zang, W.; Guan, C.; Zhang, L.; Qian, Y.; Elshahawy, A. M.; Zhao, D.; Pennycook, S. J.; Wang, J. Ni-doped cobalt−cobalt nitride heterostructure arrays for high-power supercapacitors. *ACS Energy Lett.* **2018**, *3*, 2462−2469.

(9) Liu, B.; Zhang, Q.; Wang, Z.; Li, L.; Jin, Z.; Wang, C.; Zhang, L.; Chen, L.; Su, Z. Nitrogen and sulfur-codoped porous carbon nanospheres with hierarchical icromesoporous structures and an ultralarge pore volume for high-performance upercapacitors. *ACS Appl. Mater. Interfaces* **2020**, *12*, 8225−8232.

(10) Huang, G.; Geng, Q.; Xing, B.; Liu, Y.; Li, Y.; Liu, Q.; Jia, J.; Chen, L.; Zhang, C. Manganous nitrate -assisted potassium hydroxide activation of humic acid to prepare oxygen-rich hierarchical porous carbon as high-performance supercapacitor electrodes. *J. Power Sources* **2020**, *449*, 227506.

(11) Yang, X.; Li, Y.; Zhang, P.; Sun, L.; Ren, X.; Mi, H. Hierarchical hollow carbon spheres: Novel synthesis strategy, pore structure engineering and application for micro-supercapacitor. *Carbon* **2020**, *157*, 70−79.

(12) Zhang, J.; Yang, H.; Shen, G.; Cheng, P.; Zhang, J.; Guo, S. Reduction of graphene oxide vial-ascorbic acid. *Chem. Commun.* **2010**, *46*, 1112−1114.

(13) De Silva, K. K. H.; Huang, H.-H.; Yoshimura, M. Progress of reduction of graphene oxide by ascorbic acid. *Appl. Surf. Sci.* **2018**, *447*, 338−346.

(14) Zang, P.; Gao, S.; Dang, L.; Liu, Z.; Lei, Z. Green synthesis of holey graphene sheets and their assembly into aerogel with improved ion transport property. *Electrochim. Acta* **2016**, *212*, 171−178.

(15) Sethi, M.; Bantawal, H.; Shenoy, U. S.; Bhat, D. K. Eco-friendly synthesis of porous graphene and its utilization as high performance

supercapacitor electrode material. *J. Alloys Compd.* **2019**, *799*, 256−266.
(16) Kim, D. W.; Jung, S. M.; Jung, H. Y. Long term thermostable supercapacitor using in-situ SnO_2 doped porous graphene aerogel. *J. Power Sources* **2020**, *448*, 227422.
(17) Tian, W.; Cheng, D.; Wang, S.; Xiong, C.; Yang, Q. Phytic acid modified manganese dioxide/graphene composite aerogel as high-performance electrode materials for supercapacitors. *Appl. Surf. Sci.* **2019**, *495*, 143589.
(18) Ma, Y.; Wei, N.; Wang, Q.; Wu, C.; Zeng, W.; Gao, Y.; Xu, C.; Huang, L.; Zhao, J. Ultrathin PEDOT:PSS/rGO Aerogel Providing Tape-Like Self-Healable Electrode for Sensing Space Electric Field with Electrochemical Mechanism. *Adv. Electron. Mater.* **2019**, *5*, 1900637.
(19) Su, W.; Gao, D.; Zheng, W.; Lu, F.; Liu, J.; Chen, X.; Sha, O.; Chen, L. Using carbamide for preparing nitrogen-doped graphene hydrogels to enhance supercapacitor performance. *Mater. Technol.* **2020**, *35*, 195−202.
(20) Jin, Y.; Meng, Y.; Fan, W.; Lu, H.; Liu, T.; Wu, S. Free-standing macro-porous nitrogen doped graphene film for high energy density supercapacitor. *Electrochim. Acta* **2019**, *318*, 865−874.
(21) Singh, S. K.; Dhavale, V. M.; Boukherroub, R.; Kurungot, S.; Szunerits, S. N-doped porous reduced graphene oxide as an efficient electrode material for high performance flexible solid-state supercapacitor. *Appl. Mater. Today* **2017**, *8*, 141−149.
(22) Sviridova, E.; Li, M.; Barras, A.; Addad, A.; Yusubov, M. S.; Zhdankin, V. V.; Yoshimura, A.; Szunerits, S.; Postnikov, P. S.; Boukherroub, R. Aryne cycloaddition reaction as a facile and mild modification method for design of electrode materials for high-performance symmetric supercapacitor. *Electrochim. Acta* **2021**, 137667.
(23) Thalji, M. R.; Ali, G. A. M.; Liu, P.; Zhong, Y. L.; Chong, K. F. $W_{18}O_{49}$ nanowires-graphene nanocomposite for asymmetric supercapacitors employing $AlCl_3$ aqueous electrolyte. *Chem. Eng. J.* **2021**, *409*, 128216.
(24) Moreno-Fernández, G.; Gómez-Urbano, J. L.; Enterría, M.; Cid, R.; del Amo, J. M. L.; Mysyk, R.; Carriazo, D. Understanding enhanced charge storage of phosphorus-functionalized graphene in aqueous acidic electrolytes. *Electrochim. Acta* **2020**, *361*, 136985.
(25) Gao, W.; Zhao, N.; Yao, W.; Xu, Z.; Bai, H.; Gao, C. Effect of flake size on the mechanical properties of graphene aerogels prepared by freeze casting. *RSC Adv.* **2017**, *7*, 33600−33605.
(26) Lee, S. P.; Ali, G. A. M.; Algarni, H.; Chong, K. F. Flake size-dependent adsorption of graphene oxide aerogel. *J. Mol. Liq.* **2019**, *277*, 175−180.
(27) Yang, H.; Zhang, T.; Jiang, M.; Duan, Y.; Zhang, J. Ambient pressure dried graphene aerogels with superelasticity and multifunctionality. *J. Mater. Chem. A* **2015**, *3*, 19268−19272.
(28) Qiu, L.; Liu, J. Z.; Chang, S. L. Y.; Wu, Y.; Li, D. Biomimetic superelastic graphene-based cellular monoliths. *Nat. Commun.* **2012**, *3*, 1241.
(29) Ali, G. A. M.; Divyashree, A.; Supriya, S.; Chong, K. F.; Ethiraj, A. S.; Reddy, M. V.; Algarni, H.; Hegde, G. Carbon nanospheres derived from Lablab purpureus for high performance supercapacitor electrodes: a green approach. *Dalton Trans.* **2017**, *46*, 14034−14044.
(30) Abu Bakar, N. H.; Ali, G. A. M.; Ismail, J.; Algarni, H.; Chong, K. F. Size-dependent corrosion behavior of graphene oxide coating. *Prog. Org. Coat.* **2019**, *134*, 272−280.
(31) Xu, C.; Shi, X.; Ji, A.; Shi, L.; Zhou, C.; Cui, Y. Fabrication and characteristics of reduced graphene oxide produced with different green reductants. *PLoS One* **2015**, *10*, No. e0144842.
(32) Wu, X.; Zhou, J.; Xing, W.; Wang, G.; Cui, H.; Zhuo, S.; Xue, Q.; Yan, Z.; Qiao, S. Z. High-rate capacitive performance of graphene aerogel with a superhigh C/O molar ratio. *J. Mater. Chem.* **2012**, *22*, 23186−23193.
(33) Dai, L. Functionalization of graphene for efficient energy conversion and storage. *Acc. Chem. Res.* **2013**, *46*, 31−42.
(34) Acik, M.; Lee, G.; Mattevi, C.; Pirkle, A.; Wallace, R. M.; Chhowalla, M.; Cho, K.; Chabal, Y. The role of oxygen during thermal reduction of graphene oxide studied by infrared absorption spectroscopy. *J. Phys. Chem. C* **2011**, *115*, 19761−19781.
(35) Park, S.; An, J.; Potts, J. R.; Velamakanni, A.; Murali, S.; Ruoff, R. S. Hydrazine-reduction of graphite- and graphene oxide. *Carbon* **2011**, *49*, 3019−3023.
(36) Wu, Y.; Wang, B.; Ma, Y.; Huang, Y.; Li, N.; Zhang, F.; Chen, Y. Efficient and large-scale synthesis of few-layered graphene using an arc-discharge method and conductivity studies of the resulting films. *Nano Res.* **2010**, *3*, 661−669.
(37) Shen, L.; Zhang, L.; Wang, K.; Miao, L.; Lan, Q.; Jiang, K.; Lu, H.; Li, M.; Li, Y.; Shen, B.; Zheng, W. Analysis of oxidation degree of graphite oxide and chemical structure of corresponding reduced graphite oxide by selecting different-sized original graphite. *RSC Adv.* **2018**, *8*, 17209−17217.
(38) Abbatt, J. P. D.; Bartels-Rausch, T.; Ullerstam, M.; Ye, T. J. Uptake of acetone, ethanol and benzene to snow and ice: effects of surface area and temperature. *Environ. Res. Lett.* **2008**, *3*, No. 045008.
(39) Thommes, M.; Kaneko, K.; Neimark, A. V.; Olivier, J. P.; Rodriguez-Reinoso, F.; Rouquerol, J.; Sing, K. S. W. Physisorption of gases, with special reference to the evaluation of surface area and pore size distribution (IUPAC Technical Report). *Pure Appl. Chem.* **2015**, *87*, 1051.
(40) Chaudhari, N. K.; Jin, H.; Kim, B.; Lee, K. Nanostructured materials on 3D nickel foam as electrocatalysts for water splitting. *Nanoscale* **2017**, *9*, 12231−12247.
(41) Thalji, M. R.; Ali, G. A. M.; Algarni, H.; Chong, K. F. Al^{3+} ion intercalation pseudocapacitance study of $W_{18}O_{49}$ nanostructure. *J. Power Sources* **2019**, *438*, 227028.
(42) Kim, J. H.; Byeon, M.; Jeong, Y. C.; Lee, J.; Cho, H. I.; Shin, Y. E.; Yang, S. J.; Park, C. R. Revisit to the correlation of surface characteristic nature with performance of N-enriched carbon-based supercapacitor. *Carbon* **2018**, *140*, 68−76.
(43) Zhou, Z.; Liu, T.; Khan, A. U.; Liu, G. Block copolymer−based porous carbon fibers. *Sci. Adv.* **2019**, *5*, eaau6852.
(44) Wang, J.; Polleux, J.; Lim, J.; Dunn, B. Pseudocapacitive contributions to electrochemical energy storage in TiO_2 (Anatase) nanoparticles. *J. Phys. Chem. C* **2007**, *111*, 14925−14931.
(45) Guo, X.; Yu, X.; Sun, L.; Chen, L.; Liu, C.; Zhang, S.; Wang, Z.; Chen, L.; Li, N. Electrochemically exfoliated graphene/manganese dioxide nanowire composites as electrode materials for flexible supercapacitors. *Aust. J. Chem.* **2020**, DOI: 10.1071/CH20215.
(46) Vimuna, V. M.; Athira, A. R.; Dinesh Babu, K. V.; Xavier, T. S. Simultaneous stirring and microwave assisted synthesis of nanoflakes MnO_2/rGO composite electrode material for symmetric supercapacitor with enhanced electrochemical performance. *Diamond Relat. Mater.* **2020**, *110*, 108129.
(47) Li, Q.; Chen, D.; Hu, R.; Qi, J.; Sui, Y.; He, Y.; Meng, Q.; Wei, F.; Ren, Y.; Zhao, Y.; Wei, W. Formation of hierarchical 3D cross-linked porous carbon with small addition of graphene for supercapacitors. *Int. J. Hydrogen Energy* **2020**, *45*, 27471−27481.
(48) Wang, Y.; Wang, H.; Zhang, T. C.; Yuan, S.; Liang, B. N-doped porous carbon derived from rGO-Incorporated polyphenylenediamine composites for CO2 adsorption and supercapacitors. *J. Power Sources* **2020**, *472*, 228610.
(49) Isacfranklin, M.; Yuvakkumar, R.; Ravi, G.; Hong, S. I.; Velauthapillai, D.; Thambidurai, M.; Dang, C.; Algarni, T. S.; Al-Mohaimeed, A. M. Heterostructured $SmCoO_3$/rGO composite for high-energy hybrid supercapacitors. *Carbon* **2021**, *172*, 613−623.
(50) Tarimo, D. J.; Oyedotun, K. O.; Mirghni, A. A.; Sylla, N. F.; Manyala, N. High energy and excellent stability asymmetric supercapacitor derived from sulphur-reduced graphene oxide/manganese dioxide composite and activated carbon from peanut shell. *Electrochim. Acta* **2020**, *353*, 136498.
(51) Çıplak, Z.; Yıldız, A.; Yıldız, N. Green preparation of ternary reduced graphene oxide-Au@polyaniline nanocomposite for supercapacitor application. *J. Energy Storage* **2020**, *32*, 101846.
(52) Nie, G.; Dai, S.; Deng, H.; Wang, C. Ultrafine tin dioxide nanoparticles grown on nitrogen-doped graphene with rich pyrrolic

https://dx.doi.org/10.1021/acs.energyfuels.0c04126
Energy Fuels XXXX, XXX, XXX−XXX

nitrogen for excellent supercapacitor performance. *Int. J. Electrochem. Sci.* **2020**, *15*, 8892−8900.
(53) Mei, B.-A.; Munteshari, O.; Lau, J.; Dunn, B.; Pilon, L. Physical interpretations of Nyquist plots for EDLC electrodes and devices. *J. Phys. Chem. C* **2018**, *122*, 194−206.
(54) Kang, J.; Wen, J.; Jayaram, S. H.; Yu, A.; Wang, X. Development of an equivalent circuit model for electrochemical double layer capacitors (EDLCs) with distinct electrolytes. *Electrochim. Acta* **2014**, *115*, 587−598.
(55) Kumar, P. V.; Bardhan, N. M.; Chen, G.-Y.; Li, Z.; Belcher, A. M.; Grossman, J. C. New insights into the thermal reduction of graphene oxide: Impact of oxygen clustering. *Carbon* **2016**, *100*, 90−98.
(56) Trasatti, S.; Petrii, O. A. Real surface area measurements in electrochemistry. *J. Electroanal. Chem.* **1992**, *327*, 353−376.
(57) Ali, G. A. M.; Yusoff, M. M.; Shaaban, E. R.; Chong, K. F. High performance MnO_2 nanoflower supercapacitor electrode by electrochemical recycling of spent batteries. *Ceram. Int.* **2017**, *43*, 8440−8448.

https://dx.doi.org/10.1021/acs.energyfuels.0c04126
Energy Fuels XXXX, XXX, XXX−XXX